Deriving Sea Subsurface Temperature Fields from Satellite Remote Sensing Data Using a Generative Adversarial Network Model

Jiali Zhang[1], Pengfei Ning[2], Xuefeng Zhang[3], Xidong Wang[4], and Anmin Zhang[1]

[1]Tianjin University
[2]National Marine Data and Information Service
[3]School of Marine Science and Technology, Tianjin University
[4]College of Oceanography, Hohai University

December 7, 2022

Abstract

Ingenious use of multisource satellite observations to accurately invert global and regional subsurface thermohaline structure is essential for understanding ocean interior processes, but extremely challenging. This study proposes a new method from the sea surface information inverting daily subsurface temperature (ST) based on generative adversarial network (GAN) model in China's marginal seas. The proposed GAN-based model can project the STs from sea surface information (SLA, SSTA, SST) with a high resolution of 1/12°. A traditional regression-based model, Modular Ocean Data Assimilation System (MODAS), is set up the same experiments for the sake of comparison. The results show that the averaged RMSE results are less than 1.45°C in upper 200m and the highest averaged R2 of 0.97 at the 70m level, which are better than that of MODAS. Errors analysis and typical oceanographic phenomena analysis results show the superiority of the proposed GAN-based model in this study. This study can provide high-precision daily ST data from sea surface information, which can be expanded to further studies on the ocean interior variation characteristics.

Deriving Sea Subsurface Temperature Fields from Satellite Remote Sensing Data Using a Generative Adversarial Network Model

Jiali Zhang[1], Pengfei Ning [1,2], Xuefeng Zhang [1*], Xidong Wang [3*] and Anmin Zhang [1]

[1] Marine Science and Technology, Tianjin University, Tianjin, China.

[2] National Marine Data and Information Service, Tianjin, China.

[3] Key Laboratory of Marine Hazards Forecasting, Ministry of Natural Resources, Hohai University, Nanjing, China.

Corresponding author: Xuefeng Zhang (xuefeng.zhang@tju.edu.cn)

Corresponding author: Xidong Wang (xidong_wang@hhu.edu.cn)

Key Points:

- A Generative Adversarial Network based model is proposed for deriving high-resolution daily subsurface temperature fields.
- Feature-wise loss is introduced in adversarial learning for extracting complex hydrographical characteristics from satellite observations.
- This model can accurately reflect the physical oceanographic phenomena both normal and extreme conditions.

Abstract

Ingenious use of multisource satellite observations to accurately invert global and regional subsurface thermohaline structure is essential for understanding ocean interior processes, but extremely challenging. This study proposes a new method from the sea surface information inverting daily subsurface temperature (ST) based on generative adversarial network (GAN) model in China's marginal seas. The proposed GAN-based model can project the STs from sea surface information (SLA, SSTA, SST) with a high resolution of 1/12°. A traditional regression-based model, Modular Ocean Data Assimilation System (MODAS), is set up the same experiments for the sake of comparison. The results show that the averaged RMSE results are less than 1.45°C in upper 200m and the highest averaged R2 of 0.97 at the 70m level, which are better than that of MODAS. Errors analysis and typical oceanographic phenomena analysis results show the superiority of the proposed GAN-based model in this study. This study can provide high-precision daily ST data from sea surface information, which can be expanded to further studies on the ocean interior variation characteristics.

Plain Language Summary

GANs are undoubtedly one of the most creative advances in deep learning due to their good generation performances but are not widely used for interior ocean variables' deriving. Deriving sea subsurface temperature fields from satellite remote sensing data using deep learning methods are significance but full of challenges. Most of the existing models are based on a single observation point or monthly average fields, without considering the daily fields in high spatial resolution, so they lack application value to some extent. In this study, we propose a sea surface information-guided GAN (SSIG-G) to deriving daily sea subsurface temperature fields in China's marginal seas with a high-resolution. We find that this model can more accurately reflect the typical physical oceanographic phenomena in China's marginal seas among daily, seasonally and extreme weather conditions than traditional inversion method or reanalysis data. Thus, our results indicate that the proposed SSIG-G model have great application value of real-time ocean physical phenomena researches and this study can provide methodological support for using GANs' in ocean variables' deriving.

1 Introduction

As a leading space technology, satellite remote sensing allows the observation of the state of Earth's resources and their processes at several spatial-temporal scales; for several decades, notable contributions have been made in monitoring and understanding global and regional atmospheric, ocean, and climate changes using satellite remote sensing (Yang et al., 2013; Yuan et al., 2020). Oceans have absorbed approximately 93% of the global heat entering Earth's climate system and play a decisive role in regulating and stabilizing the Earth's climate system (Johnson & Lyman, 2020; Su et al., 2021). In recent decades, the ocean heat content has significantly increased, causing global ocean warming (Boyer et al., 2016; Cheng et al., 2020; Cheng & Zhu, 2018). An improved understanding of the distribution and redistribution of heat interior ocean will help better monitor Earth's energy budget and its consequences (Drijfhout et al., 2014; Dulvy et al., 2014; Yan et al., 2016). High-precision observation data within the ocean are crucial for improving the understanding of ocean interior and subsurface thermal structures, which are highly relevant to global warming. Since making observations covering the entire

ocean with high spatial and temporal resolution is difficult, it is significant and challenging to accurately estimate ocean subsurface thermal structures based on multi-satellite remote sensing data.

Although satellite remote sensing has provided high-resolution and long time series of ocean data, its observations are confined to sea surface phenomena. Thus, most of the research on ocean interior characteristics has traditionally relied on models and in situ measurements. Extensive subsurface in situ measurement projects, such as the Integrated Ocean Observing System (IOOS) and the Global Ocean Observing System (GOOS), which adopt different observation platforms, have been established to achieve simultaneous observations of the global ocean both in time and space (Su et al., 2021; Yan et al., 2016). However, the existing subsurface observations are spatially sporadic and temporally scarce in most parts of the ocean. Studies of ocean interior characteristics are extremely limited by sparse and uneven in situ data, which leads to uncertainties in the full depth steric height from ocean interior variability analysis and prediction (Su et al., 2021; Wu et al., 2012).

The ocean surface is dynamically influenced by both the sea surface and interior ocean (e.g., thermal expansion) (Wu et al., 2012). Many subsurface phenomena have surface manifestations that can be measured and used for deriving key parameters of subsurface ocean processes, making it possible to obtain the internal parameters of the ocean from the sea surface (Klemas & Yan, 2014; Su et al., 2019). Sea surface height changes very likely reflect the traces left by sea subsurface variations, and research shows that ocean temperature is associated with thermohaline expansions that contribute substantially to sea level rise (Syst et al., 2018).

Deeper ocean remote sensing (DORS) is a technique used to obtain subsurface information from satellite measurements by using specially developed algorithms/techniques (Klemas & Yan, 2014). The DORS technique has become an important research subject because of its great potential to indirectly retrieve ocean interior information from satellite observations (Su et al., 2018). Previous studies have highlighted that the DORS technique can be used to reconstruct or invert the sea subsurface thermal structure from satellite observations mainly by using traditional dynamic and statistical methods or comprehensive dynamic and statistical methods (Fox et al., 2002; Guinehut et al., 2012; Jeong et al., 2019; Nardelli & Santoleri, 2005; Yan et al., 2020); insufficient attention has been paid to advanced machine learning approaches.

Machine learning/deep learning approaches are increasingly being used to extract patterns and insights from the ever-increasing stream of satellite remote sensing data, from which a further understanding of Earth system science problems is expected to be gained. Various forms of data-driven machine learning (ML) methods have played a valuable role in environmental remote sensing (Reichstein et al., 2019; Yuan et al., 2020). Some researchers have developed ML algorithms to estimate regional and basin-scale ocean interior thermal structures using multiple satellite observations. Backpropagation (BP) is an early ML algorithm used to retrieve subsurface temperature. Ali et al. (Ali et al., 2004) adopted the BP algorithm to estimate the subsurface temperature of the Arabian Sea by using sea surface temperature, sea surface height, wind stress, net radiation, and net heat flux. In recent years, more advanced ML algorithms have been applied to the study of ocean subsurface temperature inversion. Wu et al. (2012) developed a self-organizing map (SOM) (Wu et al., 2012) neural network to estimate subsurface temperature anomalies (STAs) in the North Atlantic by using remote sensing data and Argo gridded datasets. Su et al. (Su et al., 2015) proposed a support vector machine (SVM) method to estimate STAs in the Indian Ocean from a suite of satellite remote sensing

measurements. Su et al. (Su et al., 2018) proposed a random forest (RF)-based ML algorithm to invert STAs in the global ocean from multisource satellite observations. Lu et al. (Lu et al., 2019) reported a combined pre-clustering process and a neural network approach to determine STAs by using ocean surface temperature, surface height, surface wind observations and gridded monthly Argo data. Meng et al. (Meng et al., 2021) proposed a generative adversarial network (GAN)-based framework combined with a numerical model to predict sea subsurface temperature. In addition, popular deep learning algorithms, such as convolutional neural networks (CNNs), long short-term memory (LSTM) neural networks, extreme gradient boosting (XGBoost) and light gradient boosting machine (LightGBM), have also been adopted to invert ocean interior thermal structures from multisource satellite observations (Han et al., 2019; Su et al., 2019; Su, Wang, et al., 2021; Su, Zhang, et al., 2021).

Existing ML/DL algorithms can be used to retrieve subsurface thermal structures from sea surface parameters; while they are still in their infancy in the DORS field, they have great potential given the accumulation of ocean observation data (Su et al., 2021). In particular, there is a paucity of contributions to subsurface temperature inversion compared with sea surface temperature prediction research. Although some studies have employed advanced ML/DL algorithms in DORS, more attention was paid to estimating monthly STA fields rather than directly inferring the subsurface temperature fields from remote sensing data. In other studies, the subsurface temperature was only directly inverted at one subsurface point, not over an entire area. In addition to the deficiencies of input sea surface elements and time frequency of subsurface temperature inversion, the existing studies also lack algorithm improvements to specific research problems. Thus, there is still much room for improvement with respect to advanced ML/DL model algorithms and inversion elements in DORS. There is also room for further improvements in the accuracy of regional and basin-scale ocean interior thermohaline structures using multiple satellite observations with high resolution.

In this study, we propose a new remote sensing inversion method based on a GAN model to address the abovementioned limitations in the existing ML/DL algorithms for ST inversion. The remote sensing inversion method can be used to accurately reconstruct daily ST at 1/12◦ in China's marginal seas from multiple satellite observations, including sea surface height anomaly (SSHA), sea surface temperature (SST), sea level anomaly (SLA), and the reanalysis data products of the Hybrid Coordinate Ocean Model (HYCOM) and China Ocean Reanalysis 2.0 (CORA 2.0), for training and testing.

The remainder of the paper is organized as follows. Section 2 describes the study area and satellite observations used in this study. Section 3 presents the GAN model and proposes ST inversion via the sea surface information-guided GAN model. The experimental results and discussions are given in Section 4. Finally, Section 5 concludes the paper.

2 Study area and data

The study area covers China's marginal seas, which include the Bohai Sea (BHS), the Yellow Sea (YS) and the East China Sea (ECS) from 24°N to 41°N and from 117°E to 130°E (Fig. 1). The YS is a shallow marginal sea with an obvious seasonality of the vertical temperature structure. In winter, the temperature from the surface to the bottom in the shallow continental shelf region of the YS becomes homogeneous, while a surface boundary layer is observed in summer (Zhang et al., 2012). The BHS is the innermost gulf of the YS and is located at the western boundary of the Northwest Pacific Ocean with a maximum depth of approximately

60 m; it covers an area of approximately 78,000 km2 (Shi et al., 2011). The ECS is a typical epicontinental shelf bounding the North Pacific Ocean in the west and is connected to the YS in the north. The broad shelf of the ECS covers an area of approximately 770,000 km2. It has a mean depth of 349 m, including the narrow and deep regions of the Okinawa Trough (2100 m maximum depth). The ECS and YS are influenced by Kuroshio flows and the Northeast Asian Monsoon. The Kuroshio flows northeastward along the continental slope of the ECS with seasonal and interannual variations; the Northeast Asian Monsoon brings different air masses during the winter monsoon and the summer monsoon (Lie & Cho, 2016). The SST of the ECS has stable positions and strong seasonal variability, and the isotherms are mostly parallel to isobaths running in the southwest–northeast direction (Huang et al., 2010; Ji et al., 2018). The vertical temperature in the southern ECS is thought to have a three-layer structure, namely, an upper mixed layer, barrier layer and bottom mixed layer (Xuan et al., 2019). In this study, China's marginal seas could play an important role in modulating Pacific climate fluctuations and, to some extent, influence global climate variability. In addition, China's marginal seas have rich fishery resources. The Wentai fishing ground and Mindong fishing ground are located in the western ECS, a typical subtropical coastal ocean ecosystem (Sun et al., 2021). The Lvsi fishing ground is located at the junction of the ECS and East Yellow Sea and is the spawning ground and feeding ground of the main economic fish in the East Yellow Sea (Gao et al., 2021). The dynamics of food webs and the stability of ecosystems are key topics for studies of coastal ocean ecosystems, and mesozooplankton, which are key components in this framework, affect the stability and productivity of fish communities (Heneghan et al., 2016). The body size of an individual mesophyte as proxy for many other traits is sensitive to temperature and eutrophication and is a key factor driving trophic interactions in aquatic food webs (Sun et al., 2021; Ward et al., 2012). Therefore, understanding and predicting the thermal structures in this area is of vital importance.

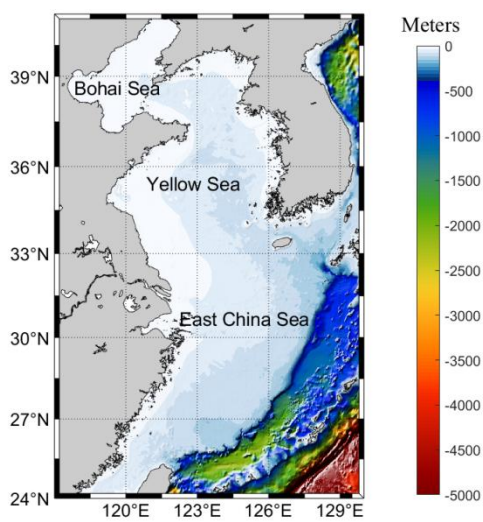

Figure. 1 Bathymetry map of China's marginal seas

The multisource satellite observations used in this study include sea-surface temperature (SST) and sea level anomaly (SLA). All the sea-surface remote sensing observations are daily data provided by the Copernicus Marine Environment Monitoring Service (CMEMS). Near real time level 4 SST products from 2007 with a spatial resolution of 0.05° × 0.05° are obtained from OSTIA (https://resources.marine.copernicus.eu/product-detail/). The SST products use in situ

and satellite data from both infrared and microwave radiometers. SLA products from 1993 with a spatial resolution of 0.25° × 0.25° are also obtained (https://resources.marine.copernicus.eu/product-detail/SEALEVEL_GLO_PHY_L4_MY_008_047/). Altimeter satellite gridded SLA data are computed based on a twenty-year mean. The SLA is estimated by optimal interpolation, merging the measurements from the different altimeter missions. There are two subsurface temperature (ST) datasets used in this experiment. The first subsurface temperature (ST) data are reanalysis data produced by the near real time Global Ocean Forecasting System (GOFS) 3.1 and are available at https://www.hycom.org/data/glbv0pt08/. This system uses the Navy Coupled Ocean Data Assimilation (NCODA) system (Cummings, 2005; Cummings and Smedstad, 2013) for data assimilation. Available satellite altimeter observations, satellites, in situ sea surface temperatures as well as other in situ observations are assimilated using this system. The ST data have a 1/12° × 1/12° horizontal spatial resolution and 41 vertical levels, but only the upper 200 m data with 13 depth levels (0, 2, 10, 15, 20, 25, 35, 50, 70, 100, 125, 150, and 200 m) are used in this study. The other ST dataset is reanalysis data produced by the National Marine Data and Information Service (NMDIS) of China (http://mds.nmdis.org.cn/). In the reanalysis data product CORA 2.0, key technologies, such as high-resolution MITgcm-CICE coupled numerical simulation and multivariable and multiscale assimilation, are adopted, and the field observation data of WOD18, GSTPP, Argo, NMDIS, satellite remote sensing observations, etc. are assimilated. The daily ST data have a 1/10° × 1/10° horizontal spatial resolution and 50 vertical levels. The depth levels used are the same as those used for the HYCOM reanalysis data product.

To train the model, the daily SST, SLA, and SSTA data from China's marginal seas are input. The SSTA is the SST anomaly with respect to the daily mean gridded SST fields. Since the sea surface parameters have different horizontal resolutions, the nearest neighbor interpolation method is adopted for all the above remote sensing variables (SST and SLA) to unify the sea surface data to a 1/12° × 1/12° horizontal resolution, which is consistent with the horizontal resolution of the ST data. To spatially match all variables, if any variable data are missing on a certain day, the day is removed and not included in model training. Then, the SST data are subtracted from their monthly averages to obtain their daily SST anomaly (SSTA) values. Similarly, the nearest neighbor interpolation method is adopted all the CORA 2.0 ST data to unify the sea surface data to a 1/12° × 1/12° horizontal resolution, and all the ST data on the upper 200 m (12 depth levels) are employed as labels for training and testing after the quality control process. Maximum–minimum normalization is applied to normalize the training and testing datasets to the range of [0,1], which ensures effective training.

For the verification of the inversion results, the measured data adopts NMDIS's Integrated Temperature & Salinity dataset (http://mds.nmdis.org.cn). The sources of this dataset include international exchange and cooperation institutions or projects and international business observations, including the observation data of China's marginal seas. After quality control, more than 300 profiles distributed in the range of 24°N-41°N and 117°E-130°E in 2018 are used in the study.

3 Methods

3.1 Generative adversarial network (GAN)

GANs are undoubtedly one of the most creative advances in deep learning (DL) in recent years (Goodfellow et al., 2014; Jozdani et al., 2022). GANs are based on the min-max, zero-sum game theory. In GAN, two neural networks are trained simultaneously in an adversarial manner: the generator (G) is used to capture the real data distribution to generate fake samples, and the discriminator (D) is used to estimate the probability that the samples originate from the real data rather than G. Competition in the training process drives both G and D to improve their performances until the generated fake data are very similar to real data, causing D to fail to distinguish generated data from real data.

GANs use the Mini-max loss function define the objective which competes in an adversarial way through a two-player minimax game as presented in Equation (1):

$$\min_G \max_D V(G,D) = \min_G \max_D E_{x\sim P_{data}(x)}[\log D(x)] + E_{x\sim P_z(z)}[1-\log D(G(z))] \quad (1)$$

The goal of G is to learn a distribution pg(x) over input data x (a prior noise distribution z ~ pz) in the space of probability density functions, so that it is possible to generate samples resemble the real data distribution pdata(x). The D is a cross-entropy classifier which aims to distinguish fake data generated by the generator from the real data x ~ Pdata. For any given G, the optimal discriminator D is shown in Equation (2):

$$D_G^*(x) = \frac{P_{data}(x)}{P_{data}(x) + P_g(x)} \quad (2)$$

The generator minimizes the Jensen–Shannon (JS) divergence to reach the goal of Pg(x) = Pdata(x) during training. When the discriminator is uncertain, the outputs of the discriminator have a probability of 1/2 whether the sample is fake or real.

Basic GANs have the advantages that Markov chains are never needed, only backpropagation is used to obtain gradients, no inference is required during learning, and a wide variety of factors and interactions can easily be incorporated into the model (Mirza & Osindero, 2014). However, it suffers from being noisy and incomprehensible by using random noise through a multilayer perceptron (MLP). The generated samples of basic GANs become uncontrollable by taking random noise as the generator's inputs, which leads to ambiguity in data generation. In addition, the locally optimal solution and gradient disappearance lead to considerable inaccuracy in the results of basic GANs.

To satisfy more high-level training goals, conditional generative adversarial nets (cGANs) were proposed by conditioning the model on additional information, such as class labels, some part of the data for inpainting or data from different modalities (Mirza & Osindero, 2014). In cGANs, the training process is supervised, and the training results are predictable. In deep convolutional generative adversarial networks (DCGANs), the popular deep learning algorithm convolutional neural networks (CNNs) (Fukushima & Miyake, 1982) were successfully combined with basic GANs for the first time (Radford et al., 2016). In DCGAN, both G and D use the architectural constraints of CNNs, which are better at image processing than MLP. As a result, stable training is achieved, and complex high-quality generators can be developed by enforcing certain constraints.

At present, basic GANs, cGANs, DCGANs and their prevalent variants have been widely used in a variety of science-related tasks, including computer vision applications (Gonog & Zhou, 2019; Isola et al., 2017; Ledig et al., n.d.; Zhu et al., 2017), video generation, prediction and remote sensing (RS) (Dash et al., 2021). Fortunately, the RS community quickly recognized the value of GANs and successfully adopted them in RS image reconstruction/restoration, RS image denoising, RS data translation and other RS-related tasks. Jozdani et al. (Jozdani et al., 2022) reviewed the relevant research on GANs in the context of RS, expecting to help the RS community understand the potential and limitations of GANs in this field. Although there have been several studies on GANs in the context of RS in recent years, remote sensing research on the applications of GANs in the ocean is still insufficient.

3.2 ST inversion via sea surface information-guided GAN (SSIG-G)

Our ultimate goal is to train a generator of a GAN-based model to generate daily ST data with typical feature representation in the study areas. In this scenario, one input to the generator is a dataset consisting of daily SST, SSTA and SSHA, and the generator is expected to invert STs from the sea surface information. In contrast to the basic GAN, the proposed GAN's generator is guided with sea surface information data as input rather than random noise, and the conditioning of the data generation process is provided by the ground truth ST data. This further motivates us to exploit a more comprehensive GAN structure, i.e., cGAN. The cGAN-based model can be used to take such conditioning inputs, which have great feature representation and generation capabilities, to address the lack of control in the basic GAN. As observed in Fig. 2 and Fig. 3, the proposed model includes two parts: 1) the SSIG generator and 2) the SSIG discriminator.

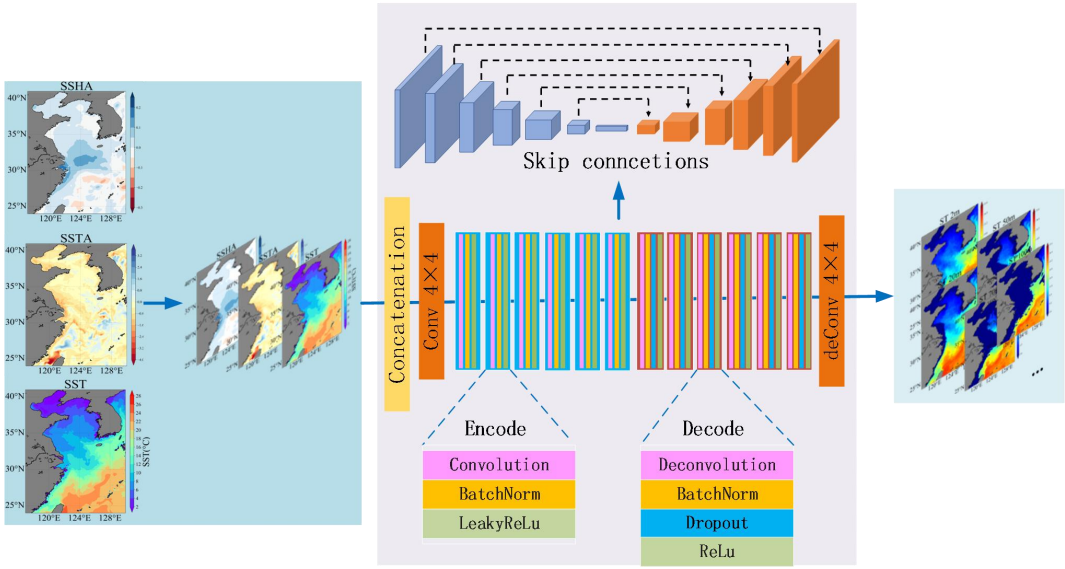

Figure 2. The structure of SSIG-generator

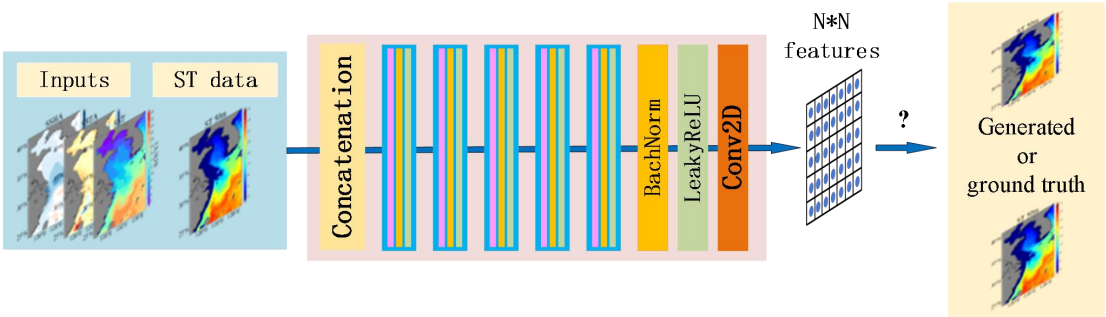

Figure 3. The structure of SSIG-discriminator.

For the SSIG generator, CNN architectures are chosen as generators to extract latent subsurface dynamic parameters because of their superiority in previous ST inversion tasks (Han et al., 2019; Su et al., 2021). The aim of the SSIG generator is to generate ST data that resembles the ground truth ST data as best as possible. The SST, SSTA and SSHA data are integrated into a concatenation method, and the SSIG generator learns a mapping from the concatenated sea surface data x to the real ST data y: G: {x, z} → y, where z represents a random noise vector, which is provided only in the form of dropout and applied on several layers of the SSIG generator (Isola et al., 2017). The SSIG generator mainly consists of three parts: 1) shallow feature extraction; 2) convolutional network modules; and 3) upsampling and reconstruction. For more high-quality inversion data, the SSIG generator is structured in terms of the U-Net deep learning structure, which is used to concatenate multilevel features between the input and output layers using skip connection (Navab et al., 2015). The SSIG generator applies six convolutional network modules (CNMs) in the following form: convolution-BatchNorm-LeakyReLU, for feature extraction, where batch normalization is used to counteract the internal covariate shift in training. Correspondingly, there are six transposed convolutional modules using ReLU as the activation function for upsampling and reconstruction.

As for the SSIG-discriminator, a convolutional "PatchGAN" classifier (Betina, 2016; Zhu et al., 2017) is chosen as discriminator to let N*N overlapping patches of inversed data can be separately taken into account. The input to SSIG-discriminator is a channel wise concatenation of the sea surface data and the corresponding generated ST (ground truth ST). Through adversarial learning, the SSIG-discriminator will not be able to discriminate the generated STs and ground truth STs. For the purpose of capturing local statistics, SSIG-discriminator convolutationally crosses the data, generating probability maps at the scale of data patches and averaging all responses to provide the ultimate output of SSIG-discriminator.

We use three different loss functions for ST inverse: adversarial loss, L1 loss and feature-wise loss. For adversarial learning, the SSIG-G adopts the adversarial loss consistent with cGAN. Adversarial loss is the key idea to GANs' success, an adversarial loss forces the generated data to be, in principle, indistinguishable from real data (Zhu et al., 2017). The objective function is given as follows:

$$L_{cGAN}(G,D) = E_{x,y}[\log D(x,y)] + E_{x,z}[\log(1 - D(x,G(x,z))] \quad (3)$$

where Ex,y represents the expectation operator with respect to x and y, G is SSIG-generator and G (x, z) learns the mapping from concatenated sea surface data x to real ST data; G is SSIG-discriminator and D (x, y) distinguishes whether x and y are the true paired data.

Flowing the previous research of a well-known cGAN model Pix2Pix (Isola et al., 2017), we use L1 loss to further improve the inversion performance. L1 loss provides an objective similarity measure between real ST and inversed ST, the loss function is defined as follows:

$$L_{L1}(G) = E_{x,y,z}[\| y - G(x,z) \|_1] \tag{4}$$

Where Ex,y,z represents the expectation operator with respect to x, y and z.

In deep generative networks, some data generation losses are optimized in a grid-based manner (grid-to-grid), so generated data typically lack high-frequency details; thus, the perceptual difference between the real data and the generated data is not understood (Kiasari et al., 2017; Wang et al., 2018). Our study area covers a large area of China's marginal seas, including the BHS, YS and ECS, with a high spatial resolution. Coupled with climate changes and offshore currents, the temperature in these areas has strong horizontal and vertical gradients (Lie & Cho, 2016; Simonyan & Zisserman, 2015). In addition, unique geographic topography and complex hydrographical characteristics are challenges for obtaining high-quality inversion ST results. To avoid undesired "blurry" inversion results in some areas with strong dynamic interactions, the proposed model needs to perceive multiscale features from other domains rather than only through a grid-to-grid approach. Inspired by image super-resolution and denoising of computer visual research, especially successes in RS image-related tasks (Ledig et al., 2017; Simonyan & Zisserman, 2015; Wang et al., 2018), we adopt a feature-wise loss by using pretrained visual geometry group (VGG) networks to capture correspondences between higher-level appearance structures, which is of great help for modeling mappings of highly complex SSI features. To fit the fixed input size of 224 × 224 × 3 of VGG-Net during training, the input data need to be resized before being fed into the network. The feature-wise loss is defined as:

$$L_{PL}(G) = \frac{1}{W_{i,j} H_{i,j}} \sum_{j=1}^{H_{i,j}} \left(\sum_{i=1}^{W_{i,j}} (\| \phi_{ij}(y) - \phi_{ij}(G(x,z)) \|_1) \right) \tag{5}$$

where ϕi,j is the feature map obtained by the j-th convolution of the well-trained VGG19 network before the i-th maxpooling layer; W is the row number of input data, and H is the column number of input data.

According to the above discussions, the overall loss function for the proposed SSIG-G is denoted as follows, where λ is the control coefficient for the relative importance of the three objectives.

$$L(G,D) = L_{cGAN}(G,D) + \lambda L_{L1}(G) + L_{PL}(G) \tag{6}$$

3.3 The Modular Ocean Data Assimilation System (MODAS)

MODAS is a modular system for ocean analysis designed to meet the U.S. Navy's need to produce rapid estimates of present and near-term ocean conditions, often in situations where little or no in situ data are available (Fox et al., 2002). Not only a static climatology, MODAS also provides a vehicle for assimilating real-time observations to provide an adjusted climatology, including remotely sensed sea surface temperature (SST) and sea surface height (SSH) data and local observations from ships, aircraft, or buoys, referred as Dynamic MODAS. As an effective traditional method, Dynamic MODAS inverses ST profiles by using stored regression relationships between remotely sensed SSH and SST data with historical temperature profile data in this area. The ocean temperature outputs of Dynamic MODAS are daily three-dimensional

gridded analysis field with grid resolution ranging from 1/2°in the open ocean to 1/8° near the coasts. In this study, MODAS's inputs are daily sea surface temperature anomaly and sea level anomaly observed by satellite, and daily subsurface temperature data in China's marginal seas is retrieved from the sea surface information. The outputs of MODAS include 50 depth levels ranging from 0 to 9000 m. The MODAS tool used in this study is from NMDIS of China.

3.4 Experimental setup

The training process consists of three steps: HYCOM reanalysis data training, fine tuning with satellite and CORA 2.0 data and model inversion. First, the SSIG-G model is trained on HYCOM ocean reanalysis data from 2000-2015 (a 15-year period), and the data from 2014 are used as the validation dataset. This training step is designed for ST inversion at each depth level (12 levels in total) by using sea surface parameter combinations (SST, SSTA, SSHA) as input. Ocean reanalysis is a reconstruction of historical and current ocean states by combining various ocean observations with a dynamical ocean model using ocean data assimilation (Han et al., 2011). As a well-known reanalysis product, HYCOM ocean reanalysis is often used to generate initial conditions for forecasts. HYCOM ocean reanalysis is used to assimilate multiple types of data (i.e., in situ temperature and salinity profiles and remotely sensed SST and altimeter sea surface height anomalies) using the Navy Coupled Ocean Data Assimilation (NCODA) three-dimensional variational data assimilation (3DVAR) technique (Jang et al., 2022). There are 5478 sets of sea surface parameter combinations (SST, SSTA, SSHA) after removing some daily combinations with poor quality grid points for one or more parameters. For a GAN-based model, it is difficult to measure the quality of generated data in an objective manner while training, as the loss value of GANs may not be indicative of the model's performance during training (Jozdani et al., 2022). The maximum number of training epochs is set to 200, and the model with the best performance on the validation dataset is saved as the final model.

Second, the trained model at each depth level was fine-tuned with satellite remote sensing data and CORA 2.0 data. Meng et al. (Meng et al., 2021) used daily Argo data to fine-tune a trained model which can improve the model performance. However, our study areas are the marginal sea of China with only a few Argo buoys at the edge of the ECS. It is difficult to adjust the model involving the whole study area using only a few observation points, especially the offshore area far away from the observation points. Therefore, we adopted satellite remote sensing data and CORA 2.0 daily data to fine tuning the entire model. CORA 2.0 data assimilated the in-site observations in China's marginal seas from the National Marine Data Information Center of China, so it has higher accuracy in our research area. Four years of CORA 2.0 daily data from 2016-2019 are used in the fine turning step, the data in 2018 is used as the testing dataset. The training setting is similar to the first step and the final models are the best performing model on validation datasets.

To evaluate the inversion accuracy, the root mean square error (RMSE) and the determination coefficient (R2) were employed as performance indexes, which are defined as follows:

$$RMSE = \sqrt{\frac{\sum_{i=1}^{n} d_i^2}{n}} \tag{7}$$

$$R^2 = 1 - \frac{\sum_{i=1}^{n}(Y_i - Y_i^{'})^2}{\sum_{i=1}^{n}(Y_i - \overline{Y})^2} \tag{8}$$

where d is the error vector calculated by the difference between the inversed STs and the field observed data, i is verification points index and n is the number of verification points; Yi represents observed STs, Yi' represents inversed STs and $\overline{Y}$ represents average of observations.

4 Results and discussion

In this study, we established the SSIG-G model to invert STs in China's marginal seas at 12 different depth levels in 2018. In this section, we first compared the inverted STs with field-observed data from NMDIS. Meanwhile, we used the traditional MODAS tool to carry out the same experiments. The experimental results were used as a benchmark to further verify the inversion accuracy of our proposed SSIG-G model. Fig. 4 and Fig. 5 and Figs. 7 to 8 show comparisons of the inversion performance of the proposed SSIG-G model and MODAS tool using different statistics and different perspectives. Next, to further verify the accuracy of the inversion results and their utility in the study of relevant oceanographic phenomena, the inversion results, MODAS results and reanalysis dataset CORA were used to analyze some typical oceanographic physical phenomena in the study areas.

4.1 Error analysis of the inversion results

Fig. 4 shows the overall inversion performances of the proposed SSIG-G model and the traditional MODAS tool for STs at 12 different depths using the average root mean square error (RMSE) and the determination coefficient (R2) as evaluation criteria. For the SSIG-G model, the average RMSE first increases from 0 to 125 m, then decreases at 150 m, and finally increases from 150 m to 200 m.

The highest inversion accuracy occurs at the top level (2 m), with the average RMSE of 0.432 °C, and the average R2 of 0.906. The lowest inversion accuracy exist in the bottom level of 200 m, with an average RMSE of 1.79 °C and an average R2 of 0.775. The highest R2 of 0.97 occurs at 70 m, and the average RMSE is 1.101 °C. For MODAS, the average RMSE variation pattern of the 12 levels is the same as that of the SSIG-G model, and the highest inversion accuracy occurs at 2 m. The average RMSE is 0.445 °C, and the average R2 is 0.897. The lowest inversion accuracy is the bottom level of 200 m, with an average RMSE of 2.152 °C and an average R2 of 0.794. At 125 m, the average RMSEs of both the SSIG-G model and MODAS are relatively high, which is due to the ST characteristics being significant and the variation range being large at this depth. The results show that for the SSIG-G model and MODAS tool, the accuracy of inversion results retrieved from sea surface information decreases gradually with increasing depth. In addition, the inversion accuracy is affected when the temperature characteristics change dramatically. Overall, we find that the inversion accuracy of the MODAS tool is not as high as that of the SSIG-G model at the 12 depth levels. The average RMSEs of the inversion results obtained by the SSIG-G model from 2-200 m are less than 2 °C, while the average RMSEs of the inversion results obtained by the MODAS tool are higher than 2 °C at 125 m and 200 m.

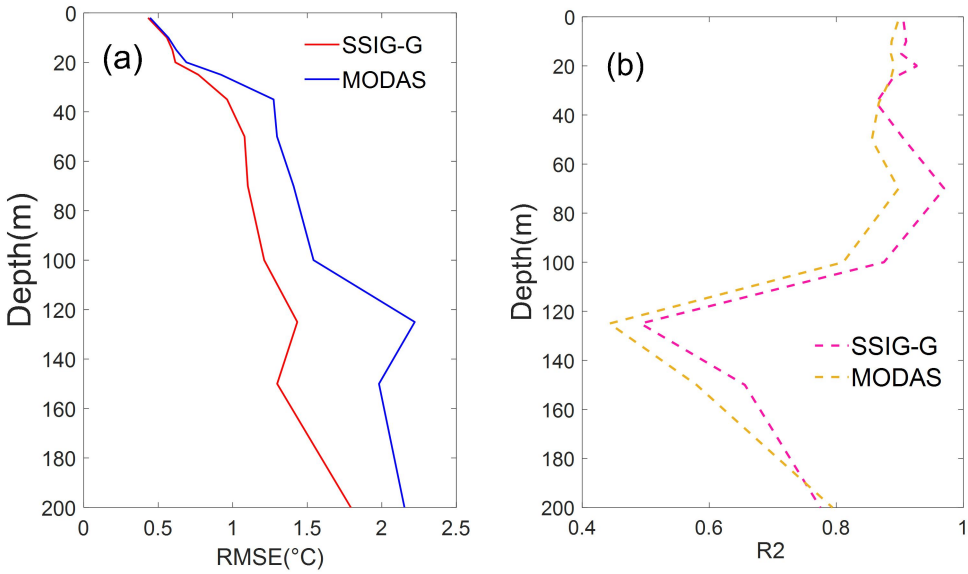

Figure 4. The performance measures of proposed model and MODAS products for STs inverse at different depths (12 levels) by employing (a) RMSE (Root Mean Squared Error) and (b) R2 (squared correlation coefficient).

Fig. 5 shows the average RMSEs of the inversion results at 12 different depths and different seasons using the proposed SSIG-G model and MODAS. Fig. 5 (a)-(d) shows the results in winter, spring, summer and autumn, respectively. We can see that the highest inversion accuracy occurs in winter; the average RMSEs at 2-200 m are less than 1.2 °C, and the inversion results of the SSIG-G model are slightly better. In winter, the cold northerly wind prevails in the study sea area, and the vertical convection mixing of sea water is very strong. In the shallow sea of the continental shelf, with a water depth of less than 100 m, the mixing depth can almost reach the seabed, resulting in a very similar plane distribution of surface and bottom water temperatures. Therefore, more accurate subsurface temperatures can be obtained from the sea surface information.

Fig. 5(b) shows that the second highest inversion accuracy occurs in spring; the average RMSEs of the SSIG-G model are less than 1.5 °C, and the lowest inverse accuracy is at 50 m. The average RMSEs of the MODAS model are less than 1.5 °C, except at 50 m. It can be inferred that the thermocline is approximately 50 m in spring in this sea area.

The lowest inversion accuracy occurs in autumn, and the average RMSEs of the SSIG-G model and MODAS are approximately 2.5 °C and 3 °C, respectively, at 200 m. In autumn, the overall pattern of STs obtained by the two methods is consistent, and the inversion accuracy decreases with increasing depth. This may be because in autumn, the water temperature distribution begins to transition to the winter type; not only does the water temperature drop significantly, but the thermocline essentially disappears, and the water temperature distribution tends to be vertically uniform. Therefore, the STs obtained by the sea surface information only show the characteristics that the accuracy decreases with increasing depth.

The inversion results in summer are shown in Fig. 5(c). The inversion accuracy of the SSIG-G model is less than 2.5 °C, and levels shallower than 100 m have an inversion accuracy below 2 °C. The inversion accuracy of MODAS is below 2.5 °C at these depth levels, except at

150 m. Although the results in summer are better than those in autumn, the inversion accuracy is much different, compared with that in winter and spring. This is because the solar radiation is strongest in summer, and the sea surface is affected by the warm and humid south wind, which is the season with the highest water temperature throughout the year. Especially during the summer monsoon, the surface water of the Yellow Sea and East China Seas is heated by the absorption of solar radiation and freshened by precipitation and freshwater discharge from land [36]. Consequently, the most prominent feature of the sea temperature distribution is that in most of the sea areas, the thermocline appears vertically, and the ST distribution pattern is very different between the surface and bottom layers. This leads to large errors in inversion STs obtained from sea surface information.

The seasonal results demonstrate that the SSIG-G model has high inversion accuracy and that the inversion results can better reflect the seasonal characteristics. Compared with the traditional MODAS tool, the SSIG-G model has a higher inversion accuracy of STs in different seasons. This indicates that the deep learning method SSIG-G has strong applicability and that the inversion results can be taken into account when studying seasonally related ocean phenomena.

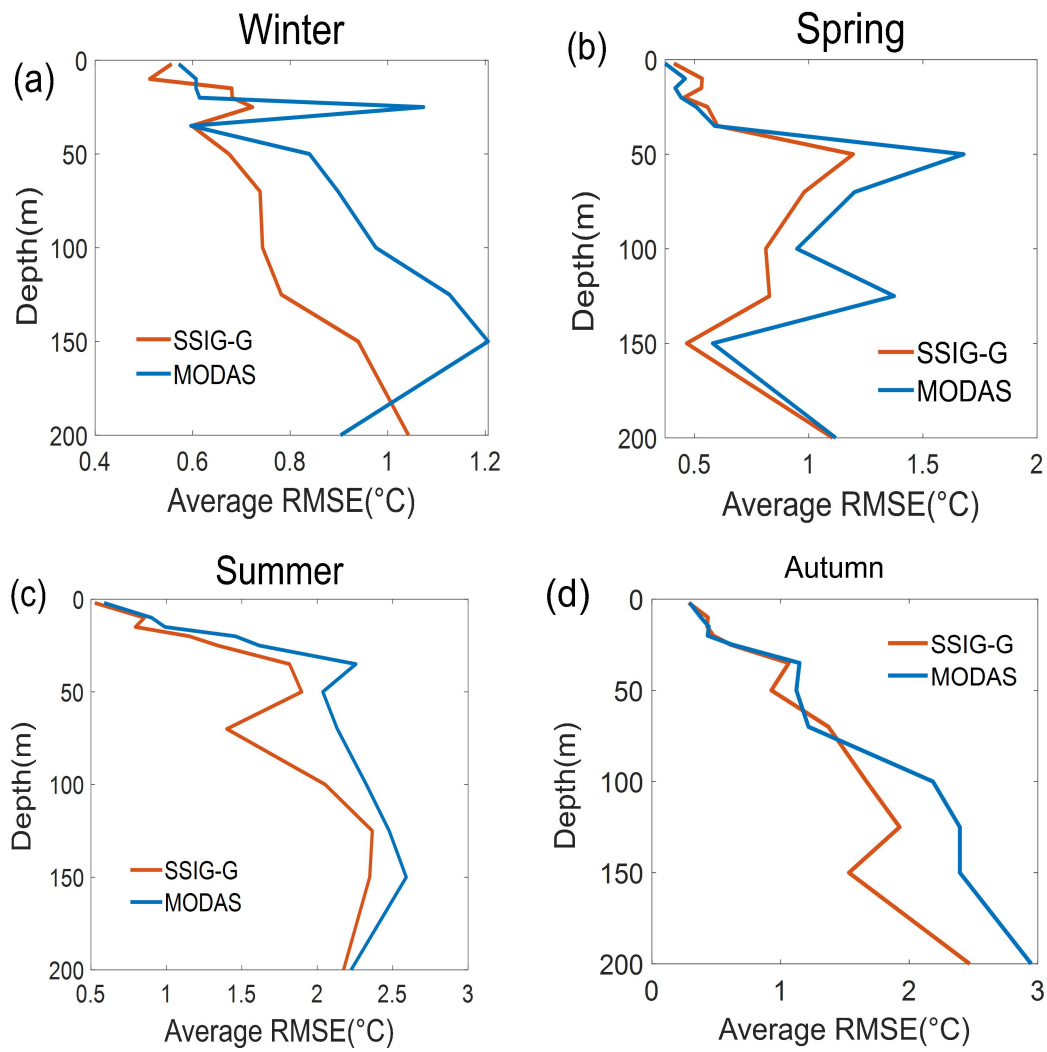

Figure 5. The average RMSEs of inversion results at 12 different depths and different seasons using the proposed SSIG-G model and MODAS, (a) winter, (b) spring, (c) summer and (d) autumn.

In order to further verify the accuracy distribution of the inversion results in the entire study area, 4 square-areas were selected throughout the study area in the experiment, namely: A, B, C, and D. Taking these 4 square-areas as verification areas, the inversion accuracy of inversion results in the whole study area is analyzed. Fig. 6 is the distribution map of observation points and schematic diagram of verification areas.

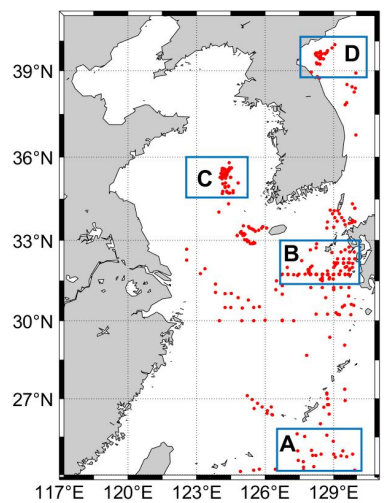

Figure 6. Distribution map of observation points and schematic diagram of verification area in 2018.

Fig.7 shows the average RMSEs of inversion results at 12 different depths in different square-areas using the proposed SSIG-G model and MODAS, Fig.7 (a)-(d) show the results in area A, B C and D respectively. We can see that square-area A has the highest inversion accuracy; the average RMSEs at 2-200m are less than 1.2 ◦C, the inversion results of SSIG-G model are slightly better. For the inversion results obtained by the two methods, the highest accuracy is 2m, and the lowest accuracy is 200m. The accuracy of 50m is higher, and the accuracy of the 70m-100m is significantly lower than that of the shallow depth levels. The accuracy of the MODAS inversion results in 70m is slightly better than that of the SSIG-G model.

The inversion results of square-area B are shown in Fig.7(b). As shown in Fig. 7(b), the inversion results accuracy of SSIG-G model is all less than 2°C, and the average RMSEs of the inversion results of 2-70m layers are 1°C or less. Fig.7(c) shows the inversion results accuracy within the square-area C. The average RMSEs of the inversion results obtained by the two methods are below 2°C, and the inversion accuracy of SSIG-G model is slightly better than that of MODAS. Fig.7(d) shows the accuracy of inversion results within the square-area D. It can be seen from this figure that the MODAS inversion results accuracy is lower at 50m, and the average RMSE exceeds 2.5°C, which is inaccurate compared with the inversion results of the SSIG-G model.

In general, the inversion result accuracy of the SSIG-G model is higher, and for some layers in some regions, the inversion result accuracy is slightly lower. This may be due to drastic changes in seasons or regions, such as the Kuroshio and California currents, and variations in the thermal structure in the upper ocean due to horizontal advection are large.

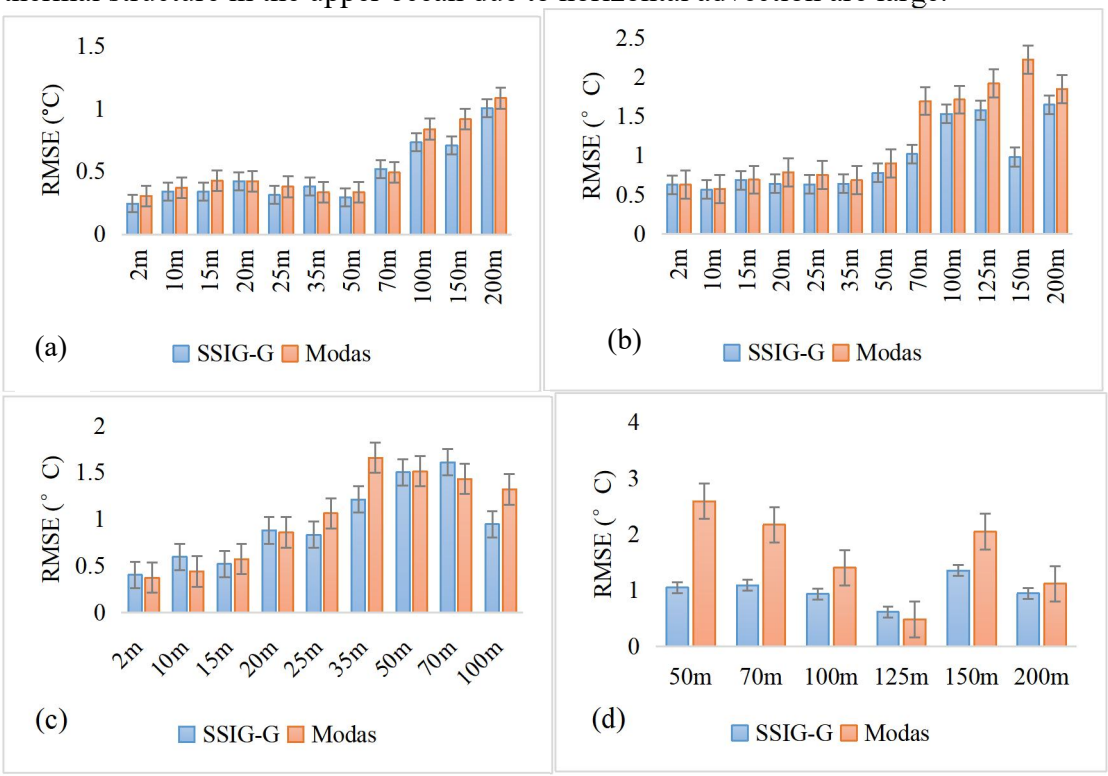

Figure 7. The average RMSEs of inversion results at 12 different depths and in different square-areas using the proposed SSIG-G model and MODAS, (a) square-area A, (b) square-area B, (c) square-area C, (d) square-area D.

Fig. 8 displays the daily error maps of STs inverted by the SSIG-G method and MODAS at 5 depth levels (10 m 35 m, 50 m, 100 m, 200 m). These error maps represent the differences between the inversion results and the field observations on June 27, 2018. The verification points on this day are mainly within the range of 27°N and 126°E, and the visual results show that the inversion STs by the SSIG-G method are closer to the ground truth observations. For example, it can be seen from Fig. 8(b), (c) and (d) that at the corresponding verification points, the errors of the SSIG-G model are obviously smaller than those of MODAS, and the errors of the other levels are small when using the SSIG-G model. The errors at the 100 m and 200 m levels are larger than those of shallower levels, which is consistent with the previous analysis results. The daily error results demonstrate that the proposed SSIG-G method is accurate.

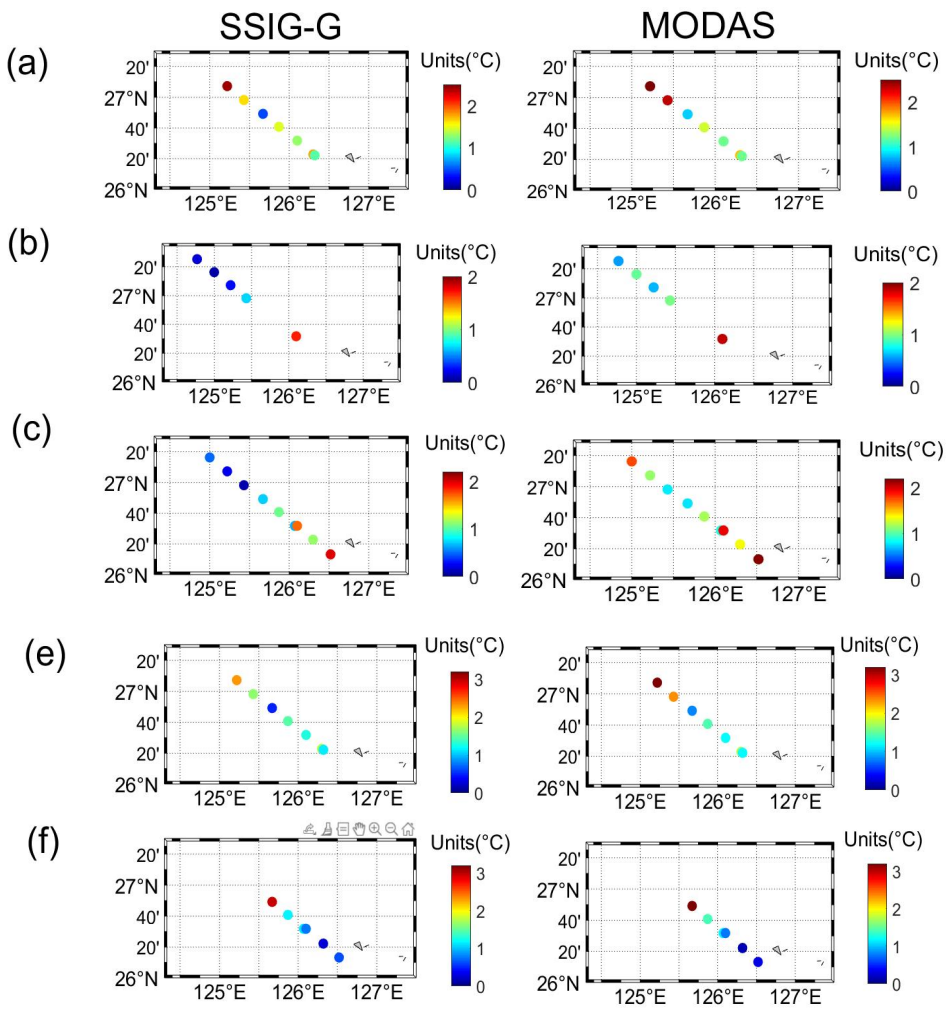

Figure 8. Daily error maps of STs inversed by the SSIG-G method and MODAS at 5 selected depths levels, on June 27, 2018; (a) 10m, (b) 35m, (c) 50m, (d) 100m and (e) 200m.

4.2 Typical physical oceanographic phenomena analysis in China's marginal seas

The temperature distribution characteristics of China's offshore and adjacent areas can be classified into three types: winter type, summer type and transitional type. In China's marginal seas, the winter type appears from December to March of the following year, when the sea temperature is the lowest throughout the year. At this time, the coastal sea temperature is low, the outer sea temperature is high, the isotherm shows a roughly parallel distribution to the coastline, and the horizontal gradient is large. The summer type, which is the season with the highest sea temperature throughout the year, appears from June to August, and the surface sea temperature generally rises. During this period, the strong solar radiation makes the sea surface temperature rise faster and the deep sea temperature rise slower. In addition, convection and eddy mixing are weak in summer, which makes the vertical distribution of sea temperature exhibit strong stratification.

The Western Pacific is the region with the highest frequency of tropical cyclones (TCs), and our research area is often affected by TCs. As a type of extreme weather, TCs have a great

impact on the upper ocean temperature in a short period. Therefore, in addition to the seasonal variation characteristics, the inversion results also need to be able to correctly reflect the temperature variations at the synoptic scale.

This section first takes summer and winter as examples to display and analyze some typical physical features of China's marginal seas through the inversion results. Then, the response of the upper ocean temperature to TCs will be further analyzed by using the SSIG-G inversion results.

4.2.1 Temperature distribution characteristics of YS

The Yellow Sea (YS) cold water mass is a typical physical oceanographic phenomenon in the shallow sea of China's continental shelf. YS cold water mass is a water body with a large temperature difference, small salt difference and low temperature as the main features. It is located at the bottom of the depression in the middle of the YS. The vertical distribution of the YS cold water mass is stratified, with three layers of structure, namely, upper and lower homogeneous layers and a thermocline. From July to August, the cold water mass reached its peak, with the strongest three-layer structure and high stability near the thermocline. Fig. 9 shows the cross-section of the YS cold water mass from the proposed SSIG-G method, MODAS and CORA in August, Fig. 9(a) shows the monthly average temperature at 35°N and Fig. 9(b) shows the monthly average temperature at 37°N. It can be seen from these figures that the vertical structure of temperature is clearly stratified, the upper sea water temperature is high and relatively evenly distributed, and below it is a strong thermocline. Most of the sea areas below the thermocline have been covered by a fully formed YS cold water mass, and the temperature is low.

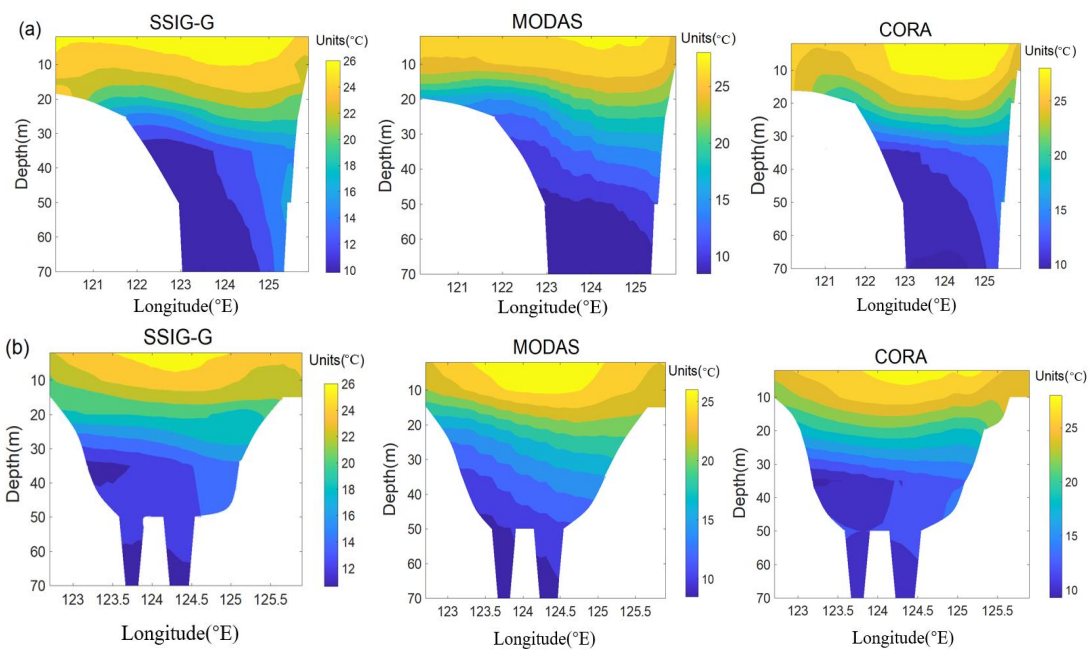

Figure 9. Monthly average temperature in August: (a) Monthly average temperature in 35°N, (b) Monthly average temperature in 37°N.

In winter, since the outer sea water entering the YS mixes with the coastal water and sinks to the deep bottom due to the cooling effect of the sea surface, the sea temperature is

vertically uniform. At this time, the northerly monsoon prevails in the sea area, and the mixing effect of eddies and convection is strong. The sea temperature distribution characteristics in the surface, middle and bottom layers of the entire YS are similar, showing the characteristics of low temperature near the coast and high temperature in the central sea. Fig. 10 shows the monthly average sea temperature of the 35°N and 37°N cross-sections in winter (February). A vertically uniform temperature can be seen clearly from this figure. The results obtained by the three methods are slightly different, but the overall characteristics are the same, which can sufficiently reflect the winter sea temperature characteristics of this sea area.

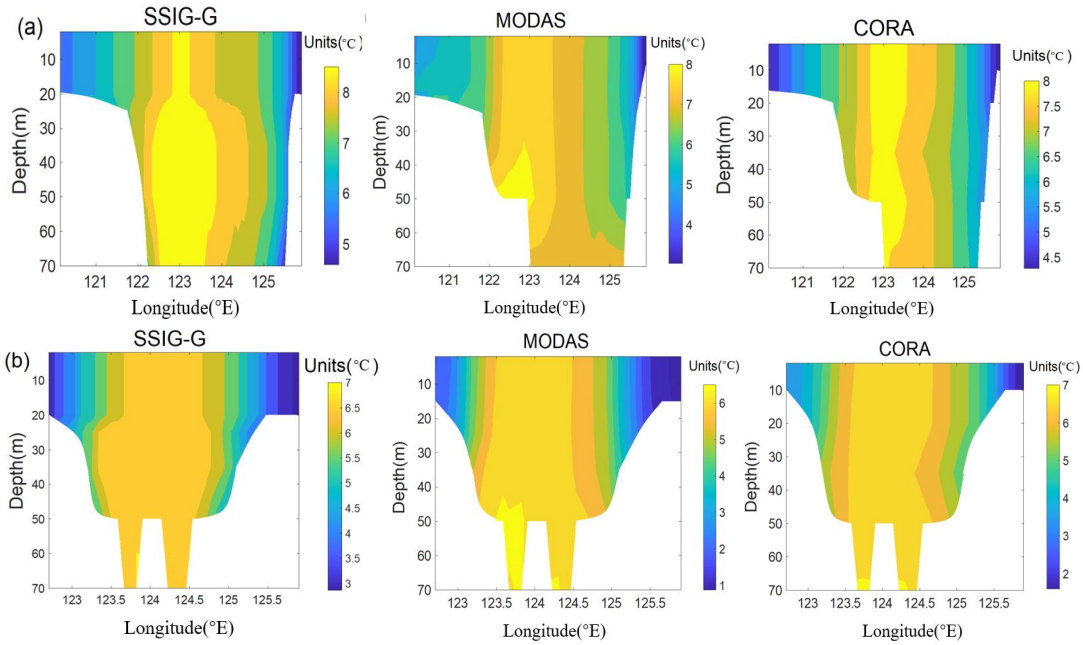

Figure 10. Monthly average temperature in February: (a) Monthly average temperature in 35°N, (b) Monthly average temperature in 37°N.

Fig. 11 shows sea temperature's horizontal distribution in summer and winter in China's marginal seas. Fig. 11(a) shows the sea temperature's horizontal distribution near the bottom of YS in summer, and the structure of YS cold water mass can be seen clearly. In particular, the SSIG-G inversion results show two obvious low temperature centers, located in the northern YS and the southern YS, respectively, which is consistent with the hydrological characteristics of this region. Fig. 11(b) shows the temperature near the bottom of the YS in winter, the temperature of the YS showed a winter characteristic at this time, without cold water mass structure.

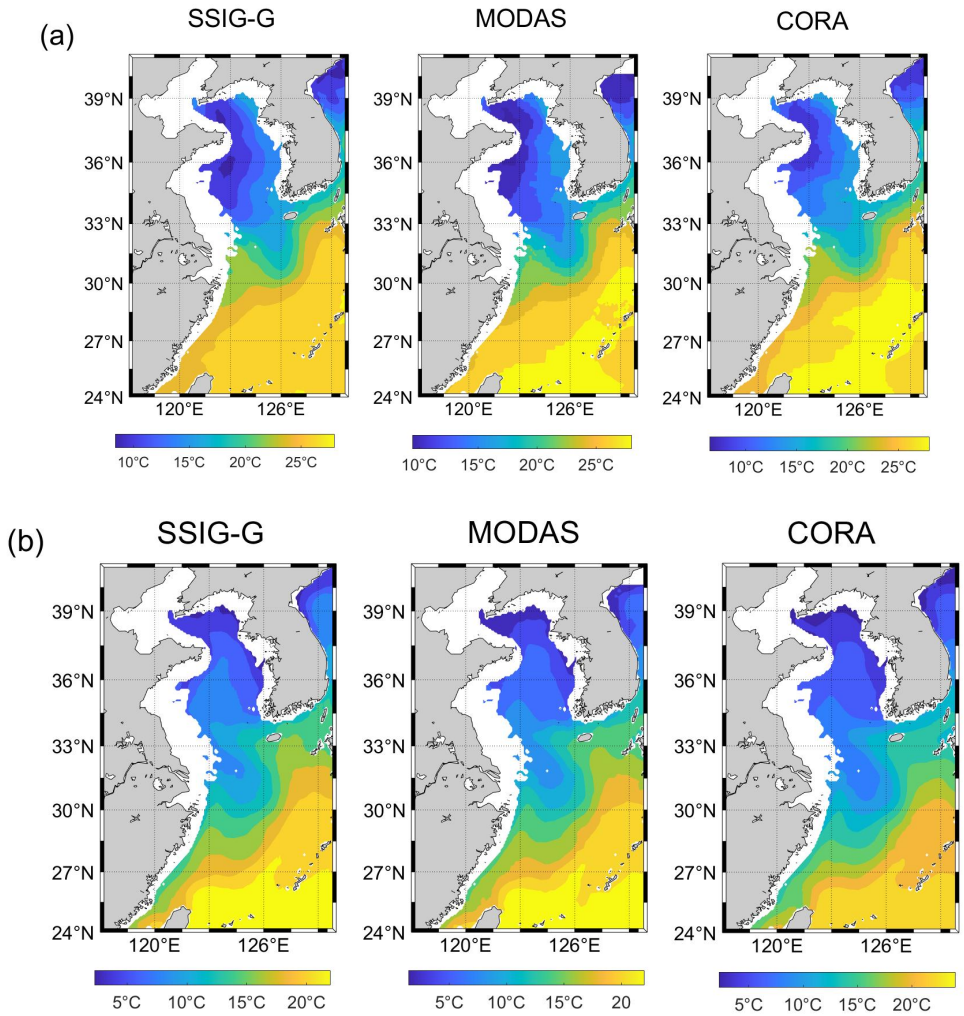

Figure 11. Monthly average sea temperature's horizontal distribution in summer and winter in China's marginal seas: (a) Monthly average sea temperature distribution near the bottom of the YS in summer, (b) Monthly average sea temperature distribution near the bottom of the YS in winter.

4.2.2 Temperature distribution characteristics of ECS

The cross-section of the ECS is selected at 31°N, which is a typical cross-section for studying the hydrological characteristics of the ECS. The sea temperature distributions in this section are different in summer and in winter. In summer, the sea temperature west of the cross-section shows a three-layer structure with increasing temperature. The sea surface temperature is above 27 °C, but there is cold water near the bottom, with a clear thermocline in the middle. In winter, the shallow water area west of this cross-section is mixed by convection directly to the seabed, and the sea temperature distribution is consistent from top to bottom. The eastern part of the cross-section is the Kuroshio high-temperature water, which shows the surface layer is above 18 °C, and the vertical distribution of sea temperature is relatively uniform to approximately 150 m. At a depth of more than 150 m, the water temperature decreases with increasing depth. The isotherm east of the section bulges upward from the seabed, and the water temperature from the

surface to the bottom drops evenly. Fig. 12 shows the 31°N cross-section results obtained by the three methods, of which Fig. 12(a) shows the results in summer. The results of the proposed SSIG-G model and CORA are similar, which proves that the inverted STs can be used to accurately reflect the physical oceanographic phenomena. The MODAS results are slightly different from those obtained by the other two methods. There is a large temperature change at 128° E, and the eastern part of the cross-section does not reflect the fact that the isotherm bulges upward well. Fig. 12(b) shows the winter results, and the three methods accurately reflect the winter temperature distribution characteristics.

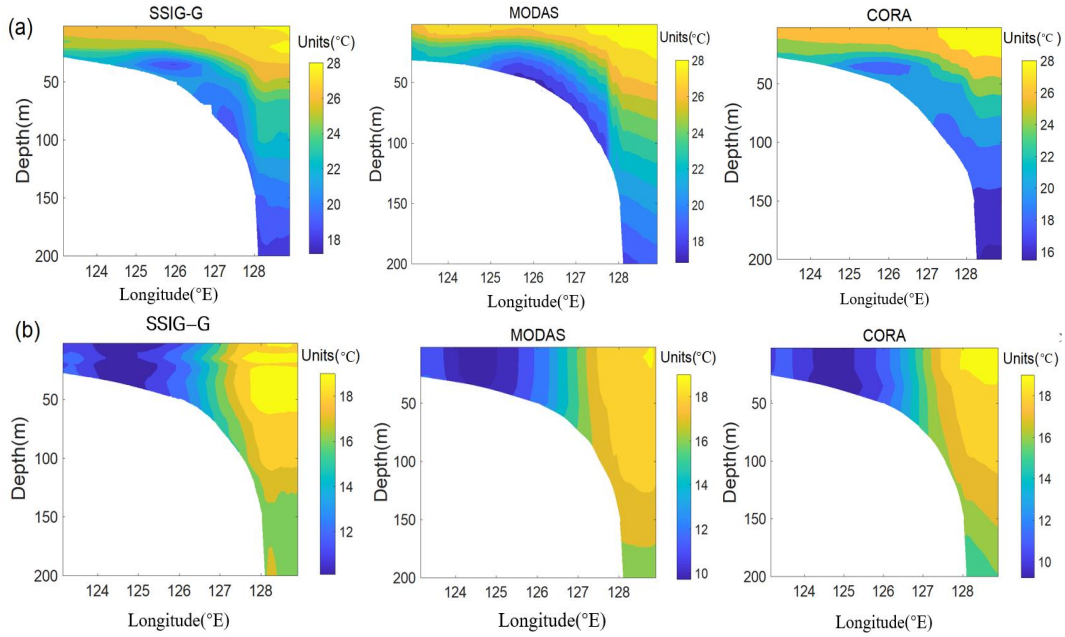

Figure 12. Monthly average temperature cross-section of the ECS in 31°N: (a) summer, (b) winter.

4.2.3 Responses of upper ocean temperature to tropical cyclones (TCs) in China's marginal seas

The ocean response and feedback to TCs are the most intense air-sea interactions involving complex processes from weather to climate scales, from local to global scales, and from dynamic and thermodynamic elements to multiple environmental variables. The specific impacts of tropical cyclones on the upper ocean are as follows: during the passage of TCs, the loss of water vapor and heat in the ocean surface, the cooling of the upper sea water and the strong wind stress and wave action can penetrate the ocean at 100-200 m depth, and thus cause turbulent mixing and strong upwelling (Chang et al., 2013). The cyclonic stress of TCs can also play a "cold suction" role in the upper ocean by the strong uplift of the ocean thermocline through Ekman suction (Chereskin & Price, 2001).

Due to the lack of in situ observations during TCs passage, response analysis of upper ocean temperature to TCs lacks sufficient data. To better verify our inversion results and further expand the applications of our inversion results in studying typical physical oceanographic phenomena in China's marginal seas, based on the China Meteorological Administration (CMA) best-track dataset (Lu et al., 2021; Ying et al., 2014) provided by the Tropical Cyclone Data Center of the CMA, four TCs that crossed China's marginal seas in 2018, "GAEMI", "YAGI", "RUMBIA" and "KONG-REY", are selected, and the response of upper ocean temperature at depths of 10-100 m during TC passage are analyzed. The sea temperature 7 days before TC

passage is taken as the reference temperature, and the responses of upper sea temperatures to TCs are analyzed by calculating the abnormal changes in sea temperature at 10 m, 50 m, 75 m and 100 m during TC passage. Fig. 13 shows the trajectory of four selected TCs in the study area.

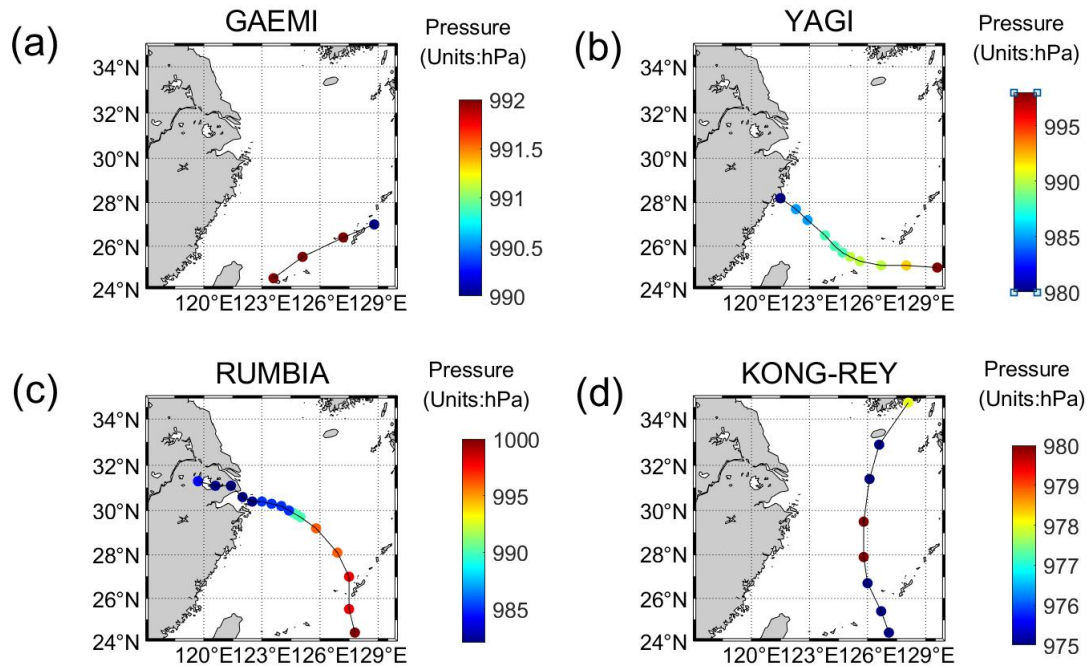

Figure 13. Trajectory of four selected TCs in the study area: (a) "GAEMI", (b) "YAGI", (c) "RUMBIA" and (d) "KONG-REY".

The trajectory of TC "GAEMI" during its passage in the study area from 12:00 on June 15 to 6:00 on June 16, 2018 is shown in Fig. 13 (a). Fig. 14 shows the abnormal temperature changes during TC "GAEMI" (June 16, 2018), and the inversion results are compared with MODAS and CORA 2.0. Fig. 14(a) - (d) show the temperature anomalies of the 10 m, 50 m, 75 m and 100 m layers, respectively. It can be seen from this figure that the CORA does not well reflect the cold anomaly of the upper ocean temperature during the transit of "GAEMI", which indicates that the reanalysis data may not well reflect the changes under the influence of weather scale without in situ observations. The inversion results of SSIG-G and MODAS obtained from satellite observations, can better reflect real-time changes. The inversion results of SSIG-G show a better cold anomaly near the "GAEMI" path.

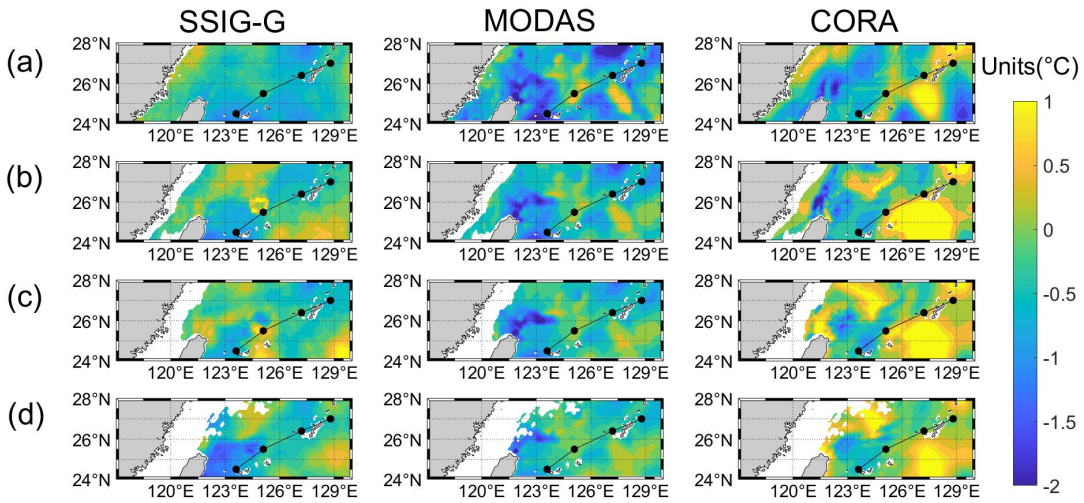

Figure 14. Temperature anomaly during the transit of TC "GAEMI" (June 16, 2018): (a) 10m, (b) 50m, (c) 75m and (d) 100m.

The trajectory of TC " YAGI " during its transit in the study area from 00:00 on August 11 to 21:00 on August 15, 2018 is shown in Fig. 13 (b) and the trajectory of TC " RUMBIA " during its transit in the study area from 12:00 on August 14 to 3:00 on August 17, 2018 is shown in Fig. 13 (c). The transit time of these two TCs overlaps, so they are analyzed together. Fig. 15 shows the abnormal temperature changes of TCs "YAGI" and "RUMBIA" during their transit (August 15, 2018). Fig. 15 (a) - (c) correspond to the temperature anomalies of 10m, 50m and 75m layers respectively. It can be seen from this figure that the results of CORA have large areas of warm anomalies in the 50m and 75m layers, which do not reflect the "cold suction" effect during the transit of TCs. The results of SSIG-G and MODAS reflect the response of the upper ocean temperature to TCs. Besides, the inversion results show warm anomalies in some regions besides cold anomalies because the subsurface temperature is also affected by the "heat pump" effect.

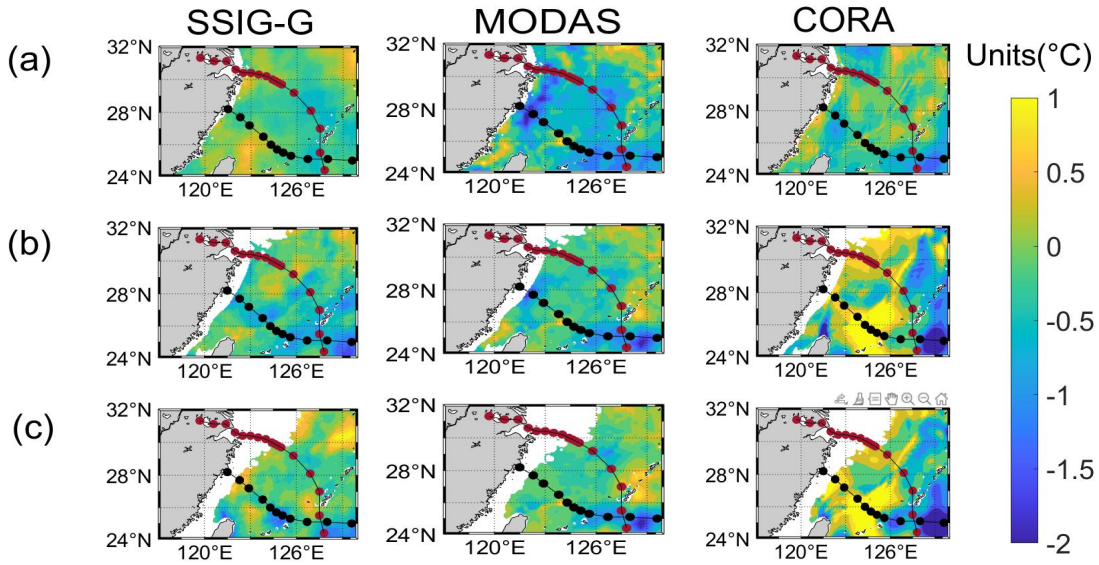

Figure 15. Temperature anomaly during the transit of TCs " YAGI "(Black dots) and "RUMBIA" (Red dots) in August 15, 2018: (a) 10m, (b) 50m, (c) 75m and (d) 100m.

The trajectory of TC "KONG-REY" during its passage in the study area from 06:00 on October 4, 2018, to 00:00 on October 6, 2018, is shown in Fig. 13(d). Fig. 16 shows the abnormal temperature changes of TC "KONG-REY" during its passage (October 5, 2018). Fig. 16(a) - (d) show the temperature anomalies at the 10 m, 50 m, 75 m and 100 m layers, respectively. Consistent with the analysis results of other TCs, the SSIG-G and MODAS results can well reflect the "cold suction" effect of TCs.

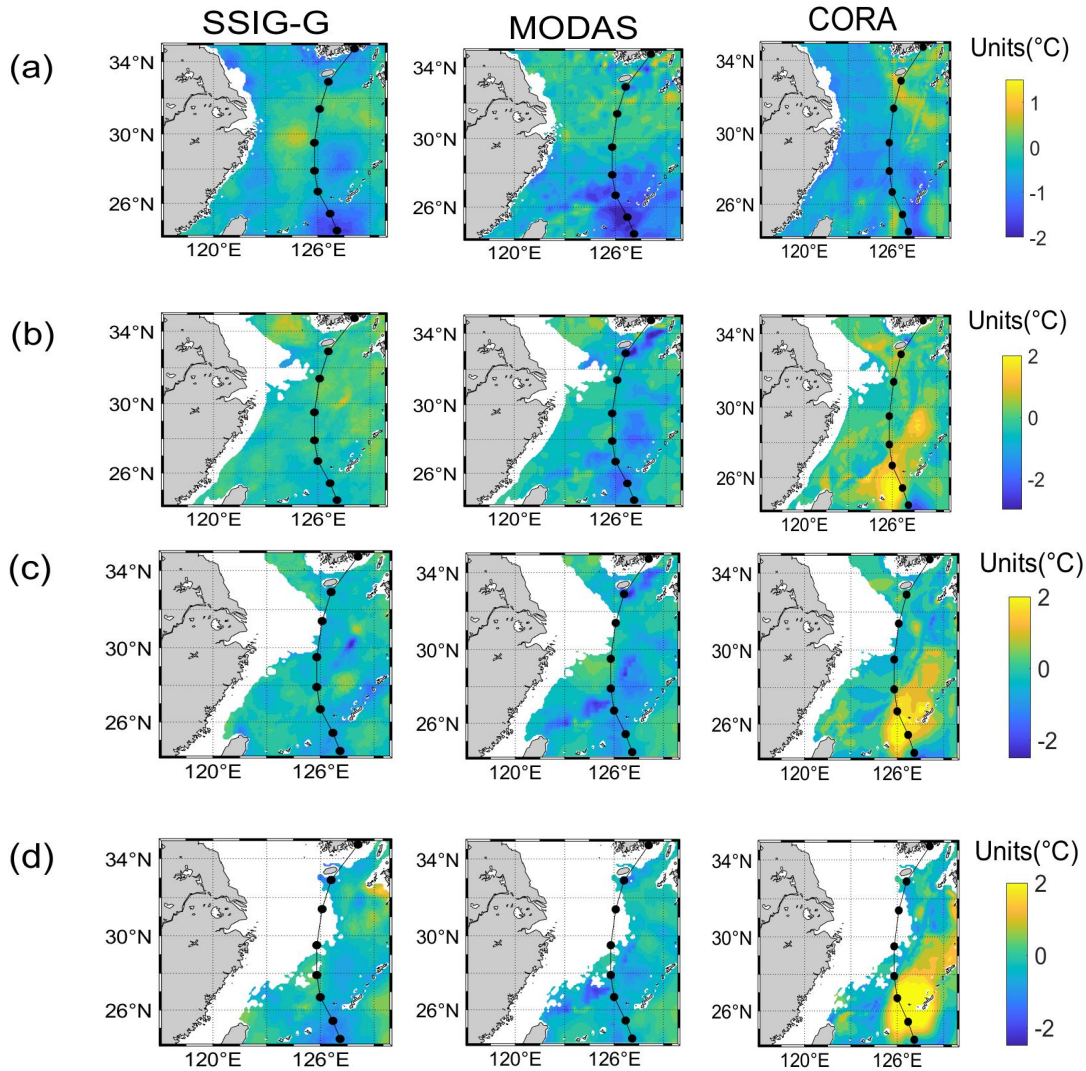

Figure 16. Temperature anomaly during the transit of TCs " KONG-REY (October 05, 2018): (a) 10m, (b) 50m, (c) 75m and (d) 100m.

5 Conclusions

In this study, a new GAN-based model was proposed for the inversion of high-resolution daily ST fields in the upper 200 m of China's marginal seas using multisource remote sensing and two reanalysis datasets. The traditional inversion tool MODAS was used for the sake of the comparison and validation. In this study, we first analyzed the inversion results at 12 different

depth levels from different temporal and spatial perspectives, including seasonal and geographical distributions, and used NMDIS's integrated temperature and salinity data for accuracy verification. Next, we further verified the inversion results and their importance in oceanographic research by analyzing the YS cold water mass and temperature distribution characteristics of the ECS in China's marginal seas.

The results show that the proposed SSIG-G model can be used to invert the daily ST fields of China's marginal seas with a resolution of 1/12°. The accuracy of the inversion results using both SSIG-G and MODAS decreases with an increase of depth, except at 125 m; the average RMSEs are less than 1.45 °C and 2.23 °C, respectively, at all depth levels, and the highest accuracy is 2 m with average RMSE of less than 0.45 °C. The highest R2 values are 0.97 and 0.898 when using the SSIG-G model and MODAS, respectively. At 70 m, the highest average R2 values of 0.97 and 0.898 are obtained using the SSIG-G model and MODAS, respectively. The results in different seasons show that the lowest inversion accuracy occurs in autumn, and the highest inversion accuracy occurs in winter. The SSIG-G model and MODAS have consistent seasonal change trends; the average RMSEs in winter are all less than 1.2 °C, while the highest average RMSEs in autumn reaches 2.5 °C and 3 °C at 200 m, respectively. The seasonal inversion results reflect the seasonal variation characteristics of China's marginal seas. For the accuracy inversion distribution results in the entire study area, the highest inversion accuracy is around square-area A, and the inversion results around square-area B is relatively poor; in square-area D, the accuracy inversion accuracy of the SSIG-G model is obviously better than that of MODAS. Overall, the SSIG-G model has higher accuracy and model robustness in both time and space.

Through the analysis of typical physical oceanographic phenomena in China's marginal seas and the comparison with MODAS and CORA, it can be seen that the inversion results obtained by the proposed SSIG-G model can accurately reflect the physical oceanographic phenomena, which has important research and application value. The vertical and horizontal distributions of the YS cold water mass in summer and winter are clearly reflected, and the unique cold water mass structure is consistent with the actual hydrological characteristics. The temperature characteristics of the ECS in summer and winter are also well reflected in the inversion results. In addition, because it is derived from satellite data, this model provides more real-time results than reanalysis data. Through the analysis of the abnormal changes of the upper ocean temperature during the passage of four tropical cyclones "GAEMI", "YAGI", "RUMBIA" and "KONG-REY", the superiority of the inversion results in this study and its application value of ocean physical phenomena researches are further verified.

Overall, the proposed SSIG-G model can take into account the spatial-temporal variation characteristics of ST structures in China's marginal seas and has higher horizontal resolution and accuracy than the traditional MODAS tool. SSHA, SSTA and SST are important sea surface information in inverting STs, and the SSIG-G model has successfully adopted these data for retrieving ocean interior thermal structures. This study can provide methodological support for the DORS technique, and the application of ML/DL in this field has once again proven to be of great value. Of course, this study uses a relatively simple framework, and more targeted improvement based on the research area and variables could be performed in the future. In addition, we can use more multisource remote sensing data and advanced ML/DL networks to improve the inversion accuracy and model robustness. Coping with ocean warming and climate change is a common issue for mankind, and abundant, multisource, massive remote sensing data

and advanced ML/DL methods have created positive impacts. Our research has provided some valuable foundations.

Acknowledgments

This work was supported by the National K&D program of China (2021YFC3101600).

Data Availability Statement

The SST and SLA data are provided by the Copernicus Marine Environment Monitoring Service (CMEMS) and are available at https://resources.marine.copernicus.eu/. The reanalysis datasets are produced by the near real time Global Ocean Forecasting System (GOFS) 3.1 (https://www.hycom.org/data/glbv0pt08/) and the National Marine Data and Information Service (NMDIS) of China (http://mds.nmdis.org.cn/). The vertification temperature profile data are provided by NMDIS of China and available at http://mds.nmdis.org.cn.

References

Ali, M. M., Swain, D., & Weller, R. A. (2004). Estimation of ocean subsurface thermal structure from surface parameters: A neural network approach. *Geophysical Research Letters*, *31*(20), 2–5. https://doi.org/10.1029/2004GL021192

Betina, V. (2016). (Improved PPF)Going Further with Point Pair Features. *Neoplasma*, *16*(1), 23–32. https://doi.org/10.1007/978-3-319-46487-9

Boyer, T., Domingues, C. M., Good, S. A., Johnson, G. C., Lyman, J. M., Ishii, M., et al. (2016). Sensitivity of global upper-ocean heat content estimates to mapping methods, XBT bias corrections, and baseline climatologies. *Journal of Climate*, *29*(13), 4817–4842. https://doi.org/10.1175/JCLI-D-15-0801.1

Chang, Y. C., Chen, G. Y., Tseng, R. S., Centurioni, L. R., & Chu, P. C. (2013). Observed near-surface flows under all tropical cyclone intensity levels using drifters in the northwestern

Pacific. *Journal of Geophysical Research: Oceans*, *118*(5), 2367–2377. https://doi.org/10.1002/jgrc.20187

Cheng, L., & Zhu, J. (2018). 2017 was the Warmest Year on Record for the Global Ocean. *Advances in Atmospheric Sciences*, *35*(3), 261–263. https://doi.org/10.1007/S00376-018-8011-Z

Cheng, L., Abraham, J., Zhu, J., Trenberth, K. E., Fasullo, J., Boyer, T., et al. (2020). Record-Setting Ocean Warmth Continued in 2019. *Advances in Atmospheric Sciences*, *37*(2), 137–142. https://doi.org/10.1007/s00376-020-9283-7

Chereskin, T. K., & Price, J. F. (2001). Ekman Transport and Pumping. In J. H. B. T.-E. of O. S. (Second E. Steele (Ed.) (pp. 222–227). Oxford: Academic Press.

Dash, A., Ye, J., & Wang, G. (2021). A review of Generative Adversarial Networks (GANs) and its applications in a wide variety of disciplines -- From Medical to Remote Sensing, *1*(1). Retrieved from http://arxiv.org/abs/2110.01442

Drijfhout, S. S., Blaker, A. T., Josey, S. A., Nurser, A. J. G., Sinha, B., & Balmaseda, M. A. (2014). Surface warming hiatus caused by increased heat uptake across multiple ocean basins. *Geophysical Research Letters*, *41*(22), 7868–7874. https://doi.org/10.1002/2014GL061456

Dulvy, N. K., Gill, J. A., Watkinson, A. R., Nash, K. L., Gill, J. A., Grant, A., et al. (2014). specific mixes of these fishes can remove sea- weeds, enhance CCA, enhance corals (6 , 9 , 12 , 33) , and replace chemical cues of degradation with chemical stimulants for recruitment., *345*(6199), 897–903.

Fox, D. N., Barron, C. N., Carnes, M. R., Booda, M., Peggion, G., & van Gurley, J. (2002). The modular ocean data assimilation system. *Oceanography*, *15*(SPL.ISS. 1), 22–28. https://doi.org/10.5670/oceanog.2002.33

Fukushima, K., & Miyake, S. (1982). Neocognitron: A Self-Organizing Neural Network Model for a Mechanism of Visual Pattern Recognition BT - Competition and Cooperation in Neural Nets. In S. Amari & M. A. Arbib (Eds.) (pp. 267–285). Berlin, Heidelberg: Springer Berlin Heidelberg.

Gao, S., Gong, S., Chen, Z., Zhang, X., Zhang, S., & Yu, W. (2021). Comparing the trophic structure of the Lvsi Fishing Ground as estimated from the Ecopath model and stable isotopic analysis. *Estuarine, Coastal and Shelf Science*, *262*(August), 107559. https://doi.org/10.1016/j.ecss.2021.107559

Gonog, L., & Zhou, Y. (2019). A review: Generative adversarial networks. *Proceedings of the 14th IEEE Conference on Industrial Electronics and Applications, ICIEA 2019*, 505–510. https://doi.org/10.1109/ICIEA.2019.8833686

Goodfellow, I. J., Pouget-Abadie, J., Mirza, M., Xu, B., Warde-Farley, D., Ozair, S., et al. (2014). Generative adversarial nets. *Advances in Neural Information Processing Systems*, *3*(January), 2672–2680. https://doi.org/10.3156/jsoft.29.5_177_2

Guinehut, S., Dhomps, A. L., Larnicol, G., & Le Traon, P. Y. (2012). High resolution 3-D temperature and salinity fields derived from in situ and satellite observations. *Ocean Science*, *8*(5), 845–857. https://doi.org/10.5194/os-8-845-2012

Han, G., Li, W., Zhang, X., Li, D., He, Z., Wang, X., et al. (2011). A regional ocean reanalysis system for coastal waters of China and adjacent seas. *Advances in Atmospheric Sciences*, *28*(3), 682–690. https://doi.org/10.1007/s00376-010-9184-2

Han, M., Feng, Y., Zhao, X., Sun, C., Hong, F., & Liu, C. (2019). A Convolutional Neural Network Using Surface Data to Predict Subsurface Temperatures in the Pacific Ocean. *IEEE Access*, *7*, 172816–172829. https://doi.org/10.1109/ACCESS.2019.2955957

Heneghan, R. F., Everett, J. D., Blanchard, J. L., & Richardson, A. J. (2016). Zooplankton are not fish: Improving zooplankton realism in size-spectrum models mediates energy transfer in food webs. *Frontiers in Marine Science*, *3*(OCT), 1–15. https://doi.org/10.3389/fmars.2016.00201

Huang, D., Zhang, T., & Zhou, F. (2010). Sea-surface temperature fronts in the Yellow and East China Seas from TRMM microwave imager data. *Deep-Sea Research Part II: Topical Studies in Oceanography*, *57*(11–12), 1017–1024. https://doi.org/10.1016/j.dsr2.2010.02.003

Isola, P., Zhu, J. Y., Zhou, T., & Efros, A. A. (2017). Image-to-image translation with conditional adversarial networks. *Proceedings - 30th IEEE Conference on Computer Vision and Pattern Recognition, CVPR 2017*, *2017-January*, 5967–5976. https://doi.org/10.1109/CVPR.2017.632

Jeong, Y., Hwang, J., Park, J., Jang, C. J., & Jo, Y. H. (2019). Reconstructed 3-D ocean temperature derived from remotely sensed sea surface measurements for mixed layer depth analysis. *Remote Sensing*, *11*(24), 1–19. https://doi.org/10.3390/rs11243018

Ji, C., Zhang, Y., Cheng, Q., Tsou, J. Y., Jiang, T., & Liang, X. S. (2018). Evaluating the impact of sea surface temperature (SST) on spatial distribution of chlorophyll-a concentration in the East China Sea. *International Journal of Applied Earth Observation and Geoinformation*, *68*(January), 252–261. https://doi.org/10.1016/j.jag.2018.01.020

Johnson, G. C., & Lyman, J. M. (2020). Warming trends increasingly dominate global ocean. *Nature Climate Change*, *10*(8), 757–761. https://doi.org/10.1038/s41558-020-0822-0

Jozdani, S., Chen, D., Pouliot, D., & Alan Johnson, B. (2022). A review and meta-analysis of generative adversarial networks and their applications in remote sensing. *International Journal of Applied Earth Observation and Geoinformation*, *108*(March). https://doi.org/10.1016/j.jag.2022.102734

Kiasari, M. A., Moirangthem, D. S., & Lee, M. (2017). Generative Moment Matching Autoencoder with Perceptual Loss. *Lecture Notes in Computer Science (Including Subseries Lecture Notes in Artificial Intelligence and Lecture Notes in Bioinformatics)*, *10635 LNCS*, 226–234. https://doi.org/10.1007/978-3-319-70096-0_24

Klemas, V., & Yan, X. H. (2014). Subsurface and deeper ocean remote sensing from satellites: An overview and new results. *Progress in Oceanography*, *122*, 1–9. https://doi.org/10.1016/j.pocean.2013.11.010

Ledig, C., Theis, L., Huszár, F., Caballero, J., Cunningham, A., Acosta, A., et al. (2017). Photo-realistic single image super-resolution using a generative adversarial network. *Proceedings - 30th IEEE Conference on Computer Vision and Pattern Recognition, CVPR 2017*, *2017-January*, 105–114. https://doi.org/10.1109/CVPR.2017.19

Lie, H. J., & Cho, C. H. (2016). Seasonal circulation patterns of the Yellow and East China Seas derived from satellite-tracked drifter trajectories and hydrographic observations. *Progress in Oceanography*, *146*, 121–141. https://doi.org/10.1016/j.pocean.2016.06.004

Lu, W., Su, H., Yang, X., & Yan, X. H. (2019). Subsurface temperature estimation from remote sensing data using a clustering-neural network method. *Remote Sensing of Environment*, *229*(September 2018), 213–222. https://doi.org/10.1016/j.rse.2019.04.009

Lu, X., Yu, H., Ying, M., Zhao, B., Zhang, S., Lin, L., et al. (2021). Western North Pacific Tropical Cyclone Database Created by the China Meteorological Administration. *Advances in Atmospheric Sciences*, *38*(4), 690–699. https://doi.org/10.1007/s00376-020-0211-7

Meng, Y., Rigall, E., Chen, X., Gao, F., Dong, J., & Chen, S. (2021). Physics-Guided Generative Adversarial Networks for Sea Subsurface Temperature Prediction. *IEEE Transactions on Neural Networks and Learning Systems*, *PP*, 1–14. https://doi.org/10.1109/tnnls.2021.3123968

Mirza, M., & Osindero, S. (2014). Conditional Generative Adversarial Nets, 1–7. Retrieved from http://arxiv.org/abs/1411.1784

Nardelli, B. B., & Santoleri, R. (2005). Methods for the reconstruction of vertical profiles from surface data: Multivariate analyses, residual GEM, and variable temporal signals in the North Pacific Ocean. *Journal of Atmospheric and Oceanic Technology*, *22*(11), 1762–1781. https://doi.org/10.1175/JTECH1792.1

Navab, N., Hornegger, J., Wells, W. M., & Frangi, A. F. (2015). Medical Image Computing and Computer-Assisted Intervention - MICCAI 2015: 18th International Conference Munich, Germany, October 5-9, 2015 proceedings, part III. *Lecture Notes in Computer Science (Including Subseries Lecture Notes in Artificial Intelligence and Lecture Notes in Bioinformatics)*, *9351*(Cvd), 12–20. https://doi.org/10.1007/978-3-319-24574-4

Radford, A., Metz, L., & Chintala, S. (2016). Unsupervised representation learning with deep convolutional generative adversarial networks. *4th International Conference on Learning Representations, ICLR 2016 - Conference Track Proceedings*, 1–16.

Reichstein, M., Camps-Valls, G., Stevens, B., Jung, M., Denzler, J., Carvalhais, N., & Prabhat. (2019). Deep learning and process understanding for data-driven Earth system science. *Nature*, *566*(7743), 195–204. https://doi.org/10.1038/s41586-019-0912-1

Shi, W., Wang, M., Li, X., & Pichel, W. G. (2011). Ocean sand ridge signatures in the Bohai Sea observed by satellite ocean color and synthetic aperture radar measurements. *Remote Sensing of Environment*, *115*(8), 1926–1934. https://doi.org/10.1016/j.rse.2011.03.015

Simonyan, K., & Zisserman, A. (2015). Very deep convolutional networks for large-scale image recognition. *3rd International Conference on Learning Representations, ICLR 2015 - Conference Track Proceedings*, 1–14.

Su, H., Wu, X., Yan, X. H., & Kidwell, A. (2015). Estimation of subsurface temperature anomaly in the Indian Ocean during recent global surface warming hiatus from satellite measurements: A support vector machine approach. *Remote Sensing of Environment*, *160*(January 2018), 63–71. https://doi.org/10.1016/j.rse.2015.01.001

Su, H., Li, W., & Yan, X. H. (2018). Retrieving Temperature Anomaly in the Global Subsurface and Deeper Ocean From Satellite Observations. *Journal of Geophysical Research: Oceans*, *123*(1), 399–410. https://doi.org/10.1002/2017JC013631

Su, H., Yang, X., Lu, W., & Yan, X. H. (2019). Estimating subsurface thermohaline structure of the global ocean using surface remote sensing observations. *Remote Sensing*, *11*(13). https://doi.org/10.3390/rs11131598

Su, H., Zhang, T., Lin, M., Lu, W., & Yan, X. H. (2021). Predicting subsurface thermohaline structure from remote sensing data based on long short-term memory neural networks. *Remote Sensing of Environment*, *260*(September 2020). https://doi.org/10.1016/j.rse.2021.112465

Su, H., Wang, A., Zhang, T., Qin, T., Du, X., & Yan, X. H. (2021). Super-resolution of subsurface temperature field from remote sensing observations based on machine learning. *International Journal of Applied Earth Observation and Geoinformation*, *102*. https://doi.org/10.1016/j.jag.2021.102440

Sun, D., Chen, Y., Feng, Y., Liu, Z., Peng, X., Cai, Y., et al. (2021). Seasonal variation in size diversity: Explaining the spatial mismatch between phytoplankton and mesozooplankton in fishing grounds of the East China Sea. *Ecological Indicators*, *131*, 108201. https://doi.org/10.1016/j.ecolind.2021.108201

Syst, E., Attribution, C. C., Global, W., Level, S., Group, B., & Cazenave, A. (2018). Global sea-level budget 1993 – present, *1*, 1551–1590.

Wang, R., Xiao, X., Guo, B., Qin, Q., & Chen, R. (2018). An effective image denoising method for UAV images via improved generative adversarial networks. *Sensors (Switzerland)*, *18*(7). https://doi.org/10.3390/s18071985

Ward, B. A., Dutkiewicz, S., Jahn, O., & Follows, M. J. (2012). A size-structured food-web model for the global ocean. *Limnology and Oceanography*, *57*(6), 1877–1891. https://doi.org/10.4319/lo.2012.57.6.1877

Wu, X., Yan, X. H., Jo, Y. H., & Liu, W. T. (2012). Estimation of subsurface temperature anomaly in the North Atlantic using a self-organizing map neural network. *Journal of Atmospheric and Oceanic Technology*, *29*(11), 1675–1688. https://doi.org/10.1175/JTECH-D-12-00013.1

Xuan, J., Su, J., Wang, H., Huang, D., Ding, R., Zhou, F., et al. (2019). Improving low-resolution models via parameterisation of the effect of submesoscale vertical advection on temperature:

A case study in the East China Sea. *Ocean Modelling*, *136*(March), 51–65. https://doi.org/10.1016/j.ocemod.2019.03.002

Yan, H., Wang, H., Zhang, R., Chen, J., Bao, S., & Wang, G. (2020). A Dynamical-Statistical Approach to Retrieve the Ocean Interior Structure From Surface Data: SQG-mEOF-R. *Journal of Geophysical Research: Oceans*, *125*(2), 1–15. https://doi.org/10.1029/2019JC015840

Yan, X. H., Boyer, T., Trenberth, K., Karl, T. R., Xie, S. P., Nieves, V., et al. (2016). The global warming hiatus: Slowdown or redistribution? *Earth's Future*, *4*(11), 472–482. https://doi.org/10.1002/2016EF000417

Yang, J., Gong, P., Fu, R., Zhang, M., Chen, J., Liang, S., et al. (2013). Erratum: The role of satellite remote sensing in climate change studies (Nature Climate Change (2013) 3 (875-883)). *Nature Climate Change*, *3*(11), 1001. https://doi.org/10.1038/nclimate2033

Ying, M., Zhang, W., Yu, H., Lu, X., Feng, J., Fan, Y. X., et al. (2014). An overview of the China meteorological administration tropical cyclone database. *Journal of Atmospheric and Oceanic Technology*, *31*(2), 287–301. https://doi.org/10.1175/JTECH-D-12-00119.1

Yuan, Q., Shen, H., Li, T., Li, Z., Li, S., Jiang, Y., et al. (2020). Deep learning in environmental remote sensing: Achievements and challenges. *Remote Sensing of Environment*, *241*(January), 111716. https://doi.org/10.1016/j.rse.2020.111716

Zhang, X., Han, G., Wang, D., Deng, Z., & Li, W. (2012). Summer surface layer thermal response to surface gravity waves in the Yellow Sea. *Ocean Dynamics*, *62*(7), 983–1000. https://doi.org/10.1007/s10236-012-0547-3

Zhu, J. Y., Park, T., Isola, P., & Efros, A. A. (2017). Unpaired Image-to-Image Translation Using Cycle-Consistent Adversarial Networks. *Proceedings of the IEEE International*

Conference on Computer Vision, *2017-October*, 2242–2251.

https://doi.org/10.1109/ICCV.2017.244